Challa S.S.R. Kumar *Editor*

Magnetic Characterization Techniques for Nanomaterials

MATERIALS.SPRINGER.COM

Springer

Magnetic Characterization Techniques for Nanomaterials

Challa S.S.R. Kumar
Editor

Magnetic Characterization Techniques for Nanomaterials

Springer

Editor
Challa S.S.R. Kumar
Integrated Mesoscale Architectures for Sustainable Catalysis (IMASC)
Rowland Institute of Science
Harvard University
Cambridge, MA, USA

ISBN 978-3-662-52779-5 ISBN 978-3-662-52780-1 (eBook)
DOI 10.1007/978-3-662-52780-1

Library of Congress Control Number: 2016953107

Printed on acid-free paper

This Springer imprint is published by Springer Nature
The registered company is Springer-Verlag GmbH Germany
The registered company address is: Heidelberger Platz 3, 14197 Berlin, Germany

Contents

1 Rotational Anisotropy Nonlinear Harmonic Generation 1
Darius H. Torchinsky and David Hsieh

2 Magnetic Rotational Spectroscopy for Probing Rheology of Nanoliter Droplets and Thin Films 51
Konstantin G. Kornev, Yu Gu, Pavel Aprelev, and Alexander Tokarev

3 Iron Oxide Nanoparticle-Based MRI Contrast Agents: Characterization and In Vivo Use 85
F. Herranz, M. P. Morales, I. Rodríguez, and J. Ruiz-Cabello

4 Nonlinear Nonequilibrium Simulations of Magnetic Nanoparticles 121
Daniel B. Reeves

5 Magnetic Force Microscopy Characterization of Magnetic Nanowires and Nanotubes 157
Muhammad Ramzan Tabasum, Fatih Zighem, Luc Piraux, and Bernard Nysten

6 Characterization of Magnetism in Gold Nanoparticles 191
B. Donnio, J. L. Gallani, and M. V. Rastei

7 Magnetic Force Microscopy 209
Daniele Passeri, Livia Angeloni, Melania Reggente, and Marco Rossi

8 Characterization of Magnetic Hyperthermia in Magnetic Nanoparticles 261
Eva Natividad and Irene Andreu

9 In Situ Lorentz Microscopy and Electron Holography Magnetization Studies of Ferromagnetic Focused Electron Beam Induced Nanodeposits 305
César Magén, Luis A. Rodríguez, Luis E. Serrano-Ramón, Christophe Gatel, Etienne Snoeck, and José M. De Teresa

10 Neutron Reflectivity to Characterize Nanostructured Films 339
Sirshendu Gayen, Milan K. Sanyal, and Max Wolff

11 Characterization of Magnetism in Core–Shell Nanoparticles 375
Elizabeth Skoropata and Johan van Lierop

12 Characterization of Ferromagnetic Bimetallic Nanomaterials Using Electron Microscopy 413
Nabraj Bhattarai

13 Magnetic Characterization of Nanodendritic Platinum 431
Wenxian Li, Ziqi Sun, and Shi-Xue Dou

14 Magneto-Optical (MO) Characterization Tools for Chemically Prepared Magnetic Nanomaterials 457
Francesco Pineider and Claudio Sangregorio

15 Magnetic Nanoparticles Used as Contrast Agents in MRI: Relaxometric Characterisation 511
Marc-André Fortin

Index 557

Contributors

Irene Andreu Instituto de Ciencia de Materiales de Aragón (ICMA), CSIC - Universidad de Zaragoza, Zaragoza, Spain

Livia Angeloni Department of Basic and Applied Sciences for Engineering, SAPIENZA University of Rome, Rome, Italy

Pavel Aprelev Department of Materials Science and Engineering, Clemson University, Clemson, SC, USA

Nabraj Bhattarai Emergent Atomic and Magnetic Structures, Division of Materials Sciences and Engineering, Ames Laboratory, Ames, IA, USA

José M. De Teresa Laboratorio de Microscopias Avanzadas (LMA), Instituto de Nanociencia de Aragón (INA), Zaragoza, Spain

Departamento de Física de la Materia Condensada, Instituto de Ciencia de Materiales de Aragón (ICMA), Universidad de Zaragoza-CSIC, Zaragoza, Spain

Transpyrenean Associated Laboratory for Electron Microscopy (TALEM), CEMES-INA, CNRS-Universidad de Zaragoza, Zaragoza, Spain

B. Donnio IPCMS-DMO, CNRS – University of Strasbourg, Strasbourg, France

Shi-Xue Dou Institute for Superconducting and Electronic Materials, University of Wollongong, Wollongong, NSW, Australia

Marc-André Fortin Laboratory for Biomaterials in Imaging, Axe médecine régénératrice, Centre de recherche du Centre hospitalier universitaire de Québec (CR-CHUQ), Quebec City, QC, Canada

Département de génie des mines, de la métallurgie et des matériaux and Centre de recherche sur les matériaux avancés (CERMA), Université Laval, Quebec City, QC, Canada

J. L. Gallani IPCMS-DMO, CNRS – University of Strasbourg, Strasbourg, France

Christophe Gatel Centre d'Élaboration de Matériaux et des Etudes Structurales (CEMES-CNRS), Toulouse, France

Transpyrenean Associated Laboratory for Electron Microscopy (TALEM), CEMES-INA, CNRS-Universidad de Zaragoza, Zaragoza, Spain

Sirshendu Gayen Surface Physics and Material Science Division, Saha Institute of Nuclear Physics, Kolkata, India

Yu Gu Department of Materials Science and Engineering, Clemson University, Clemson, SC, USA

F. Herranz Advanced Imaging Unit, Centro Nacional de Investigaciones Cardiovasculares Carlos III (CNIC) and CIBERES, Madrid, Spain

David Hsieh Department of Physics, California Institute of Technology, Pasadena, CA, USA

Konstantin G. Kornev Department of Materials Science and Engineering, Clemson University, Clemson, SC, USA

Wenxian Li School of Materials Science and Engineering, Shanghai University, Shanghai, People's Republic of China

Institute for Superconducting and Electronic Materials, University of Wollongong, Wollongong, NSW, Australia

César Magén Laboratorio de Microscopias Avanzadas (LMA), Instituto de Nanociencia de Aragón (INA), Zaragoza, Spain

Departamento de Física de la Materia Condensada, Universidad de Zaragoza, Zaragoza, Spain

Fundación ARAID, Zaragoza, Spain

Transpyrenean Associated Laboratory for Electron Microscopy (TALEM), CEMES-INA, CNRS-Universidad de Zaragoza, Zaragoza, Spain

Departamento de Física, Universidad del Valle, Cali, Colombia

M. P. Morales Instituto de Ciencia de Materiales de Madrid (ICMM)/CSIC, Cantoblanco, Spain

Eva Natividad Instituto de Ciencia de Materiales de Aragón (ICMA), CSIC - Universidad de Zaragoza, Zaragoza, Spain

Bernard Nysten Institute of Condensed Matter and Nanosciences, Bio and Soft Matter (IMCN/BSMA), Université catholique de Louvain, Louvain La Neuve, Belgium

Daniele Passeri Department of Basic and Applied Sciences for Engineering, SAPIENZA University of Rome, Rome, Italy

Francesco Pineider INSTM and Department of Chemistry and Industrial Chemistry, University of Pisa, Pisa, Italy

Luc Piraux Institute of Condensed Matter and Nanosciences, Bio and Soft Matter (IMCN/BSMA), Université catholique de Louvain, Louvain La Neuve, Belgium

M. V. Rastei IPCMS-DMO, CNRS – University of Strasbourg, Strasbourg, France

Daniel B. Reeves Department of Physics and Astronomy, Dartmouth College, Hanover, NH, USA

Vaccine and Infectious Disease Division, Fred Hutchinson Cancer Research Center, Seattle, WA, USA

Melania Reggente Department of Basic and Applied Sciences for Engineering, SAPIENZA University of Rome, Rome, Italy

Luis A. Rodríguez Laboratorio de Microscopias Avanzadas (LMA), Instituto de Nanociencia de Aragón (INA), Zaragoza, Spain

Departamento de Física de la Materia Condensada, Universidad de Zaragoza, Zaragoza, Spain

Centre d'Élaboration de Matériaux et des Etudes Structurales (CEMES-CNRS), Toulouse, France

Transpyrenean Associated Laboratory for Electron Microscopy (TALEM), CEMES-INA, CNRS-Universidad de Zaragoza, Zaragoza, Spain

I. Rodríguez Department of Physical Chemistry, Faculty of Pharmacy, Complutense University, Madrid, Spain

Advanced Imaging Unit, Centro Nacional de Investigaciones Cardiovasculares Carlos III (CNIC) and CIBERES, Madrid, Spain

Marco Rossi Department of Basic and Applied Sciences for Engineering, SAPIENZA University of Rome, Rome, Italy

Centro di Ricerca per le Nanotecnologie Applicate all'Ingegneria della Sapienza (CNIS), SAPIENZA University of Rome, Rome, Italy

J. Ruiz-Cabello Department of Physical Chemistry, Faculty of Pharmacy, Complutense University, Madrid, Spain

Advanced Imaging Unit, Centro Nacional de Investigaciones Cardiovasculares Carlos III (CNIC) and CIBERES, Madrid, Spain

Claudio Sangregorio INSTM and ICCOM-CNR, Sesto Fiorentino (FI), Italy

Milan K. Sanyal Surface Physics and Material Science Division, Saha Institute of Nuclear Physics, Kolkata, India

Luis E. Serrano-Ramón Centre d'Élaboration de Matériaux et des Etudes Structurales (CEMES-CNRS), Toulouse, France

Transpyrenean Associated Laboratory for Electron Microscopy (TALEM), CEMES-INA, CNRS-Universidad de Zaragoza, Zaragoza, Spain

Elizabeth Skoropata Department of Physics and Astronomy, University of Manitoba, Winnipeg, MB, Canada

Etienne Snoeck Centre d'Élaboration de Matériaux et des Etudes Structurales (CEMES-CNRS), Toulouse, France

Transpyrenean Associated Laboratory for Electron Microscopy (TALEM), CEMES-INA, CNRS-Universidad de Zaragoza, Zaragoza, Spain

Ziqi Sun Institute for Superconducting and Electronic Materials, University of Wollongong, Wollongong, NSW, Australia

School of Chemistry, Physics and Mechanical Engineering, Queensland University of Technology Gardens Point, Brisbane, QLD, Australia

Muhammad Ramzan Tabasum Institute of Condensed Matter and Nanosciences, Bio and Soft Matter (IMCN/BSMA), Université catholique de Louvain, Louvain La Neuve, Belgium

Alexander Tokarev Department of Materials Science and Engineering, Clemson University, Clemson, SC, USA

Darius H. Torchinsky Department of Physics, California Institute of Technology, Pasadena, CA, USA

Temple University Department of Physics and Temple Materials Institute, Temple University, Philadelphia, PA, USA

Johan van Lierop Department of Physics and Astronomy, University of Manitoba, Winnipeg, MB, Canada

Max Wolff Department of Physics and Astronomy, Uppsala University, Uppsala, Sweden

Fatih Zighem LSPM, CNRS-Université Paris 13, Sorbonne Paris Cité, Villetaneuse, France

Rotational Anisotropy Nonlinear Harmonic Generation

1

Darius H. Torchinsky and David Hsieh

Contents

1 Definition of the Subject 1
2 Overview 2
3 Introduction 2
4 Experimental and Instrumental Methodology 3
4.1 The Nonlinear Optical Response of Crystals 3
4.2 Optical Setups 7
5 Key Research Findings 12
5.1 Crystallographic Measurements of Hard Condensed Matter 12
5.2 Electronic Effects and Magnetic Order in Hard Condensed Matter 26
6 Conclusions and Future Perspective 36
References 38

1 Definition of the Subject

Rotational anisotropy nonlinear harmonic generation (RA-NHG) is an all-optical technique by which crystallographic, magnetic, and electronic symmetries of crystalline materials' bulk surface and interfaces may be examined. It also allows characterization of nanostructures and biological tissue as well as imaging

D.H. Torchinsky (✉)
Department of Physics, California Institute of Technology, Pasadena, CA, USA

Present Address:
Temple University Department of Physics and Temple Materials Institute, Temple University, Philadelphia, PA, USA
e-mail: dtorchin@temple.edu

D. Hsieh
Department of Physics, California Institute of Technology, Pasadena, CA, USA
e-mail: dhsieh@caltech.edu

C.S.S.R. Kumar (ed.), *Magnetic Characterization Techniques for Nanomaterials*,
DOI 10.1007/978-3-662-52780-1_1

applications. In this chapter, we describe the principles behind RA-NHG, discuss current experimental approaches, and review key experimental findings since 2009.

2 Overview

The lattice and electronic symmetries of a crystalline material lie at the core of its physical properties. In recent years, rotational anisotropy nonlinear harmonic generation (RA-NHG) has established itself as a complementary technique to the diffraction-based probes used to determine these symmetries. As it is based on tabletop sources, RA-NHG may be interfaced with imaging modalities and femtosecond spectroscopies to provide unique information through time and spatially resolved measurements of material symmetry.

Here we describe RA-NHG in depth, beginning with a brief review of the theory behind the technique and its basis in crystal symmetry. We discuss technical details of how the method is applied in practice. We also illustrate how RA-NHG can probe the crystallographic and magnetic properties of a wide variety of systems, using selections from the most recent literature as examples. The reviewed topics include, but are not limited to, structural refinement of centrosymmetric crystals, nonlinear optical super-resolution imaging of chiral nanoparticles, and real-time observations of the interplay between the various degrees of freedom in multiferroics.

3 Introduction

Symmetry forms the basis for our understanding of the bulk mechanical, electrical, and magnetic properties of crystalline materials. While diffraction-based probes are powerful and well-established approaches for characterizing symmetry, nonlinear optical generation offers many complementary and unique capabilities. Nonlinear optics is nondestructive; can be performed on small samples, in a variety of sample environments including low temperatures and magnetic fields; and can be interfaced with out-of-equilibrium time-domain experiments. The inherent versatility of optical methods allows their application to a variety of fields.

At the heart of this approach is the anisotropy of the nonlinear optical response either as a function of the rotation angle of the polarization of the incoming and emitted harmonic generated light or as a function of rotation of the sample itself with respect to the light-scattering plane. The general measurement of this angle-dependent nonlinear optical response is called rotational anisotropy nonlinear harmonic generation (RA-NHG). Depending upon the geometry and material property being probed, second (RA-SHG) or third (RA-THG) harmonic may be measured, although even higher harmonics can be accessed. As we show below, much can be learned about the crystalline, electric, and magnetic properties of a material when the origin of the RA-NHG is properly modeled, ranging from structural refinement of bulk single crystals to stacking angles of 2D materials, to the influence of excitonic states on optical properties, and to adsorbed molecular motion.

There have been a number of excellent books and reviews on the basics and applications of nonlinear optics [9, 15, 19, 33, 44, 48, 68, 131, 155, 164, 173, 174, 218], including specifically for RA-SHG [38, 53, 101, 132], and we refer the reader to these sources for a broad introduction. Our focus will be split between a brief review of the basic theory, a description of the currently employed experimental configurations, and an overview of the experimental findings. Our review will complement the existing literature through concentrating on new results published from 2009 onward.

We begin by elaborating on the mechanism by which the nonlinear optical response encodes the structural, electronic, and magnetic symmetries of a crystalline system in Sect. 2.1. Then we describe the variety of RA-NHG techniques and geometries currently employed in Sect. 2.2. We then review the advances in the application of this technique to magnetic and nonmagnetic solids in Sect. 3.1. Specific examples are discussed to highlight the myriad applications of RA-NHG.

4 Experimental and Instrumental Methodology

4.1 The Nonlinear Optical Response of Crystals

In this section, we review the origin of the nonlinear optical response and its application to the study of solids. We begin by considering an electric field $E_i(\mathbf{r}, t)$ of polarization $i(= x, y, z)$ at position $\mathbf{r}$ and time t radiated due to the interaction of an incident field with a medium. This radiated field $E_i(\mathbf{r}, t)$ is given by the inhomogeneous wave equation

$$\left(\nabla^2 - \frac{1}{c^2}\frac{\partial^2}{\partial t^2}\right)E_i(\mathbf{r}, t) = S_i(\mathbf{r}, t), \tag{1.1}$$

where c is the speed of light and $S_i(\mathbf{r}, t)$ is the induced source in the sample generated by the incident field. In the plane wave approximation, $E_i(\mathbf{r}, t) = E_0 e^{-i(\mathbf{k}\cdot\mathbf{r}-\omega t)}$, and the radiated field strength is proportional to the induced sources. To the lowest order in the multipole expansion, $S_i(\mathbf{r}, t)$ is given by

$$S_i(\mathbf{r}, t) = \mu_0 \frac{\partial^2 P_i(\mathbf{r}, t)}{\partial t^2} + \mu_0\left(\varepsilon_{ijk}\nabla_j \frac{\partial M_k(\mathbf{r}, t)}{\partial t}\right) - \mu_0\left(\nabla_j \frac{\partial^2 Q_{ij}(\mathbf{r}, t)}{\partial t^2}\right) \tag{1.2}$$

where μ_0 is the vacuum permeability, $P_i(\mathbf{r}, t)$ is the induced polarization (electric dipole moment/unit volume) of the medium, ε_{ijk} is the Levi-Civita symbol, $M_i(\mathbf{r}, t)$ is the induced magnetization (magnetic dipole moment/unit volume), and $Q_{ij}(\mathbf{r}, t)$ is the induced quadrupolar density.

Each source term in Eq. 1.2 may be expanded in powers of the incident radiation, more easily expressed in the frequency domain through $P(\mathbf{r}, t) = \int_{\infty}^{\infty} \tilde{P}(\mathbf{r}, \omega) e^{i\omega t} d\omega$. Both the electric and magnetic components of the incident radiation can interact with the sample. Dropping the arguments and tildes for notational convenience, we obtain

$$P_i \propto \chi_{ij}^{ee} E_j + \chi_{ij}^{em} H_j + \chi_{ijk}^{eee} E_j E_k + \chi_{ijk}^{eem} E_j H_k + \chi_{ijk}^{emm} H_j H_k + \ldots \tag{1.3}$$

$$M_i \propto \chi_{ij}^{me} E_j + \chi_{ij}^{mm} H_j + \chi_{ijk}^{mee} E_j E_k + \chi_{ijk}^{mem} E_j H_k + \chi_{ijk}^{mmm} H_j H_k + \ldots \tag{1.4}$$

and

$$Q_{ij} \propto \chi_{ijk}^{qe} E_k + \chi_{ijk}^{qm} H_k + \chi_{ijkl}^{qee} E_k E_l + \chi_{ijkl}^{qem} E_k H_l + \chi_{ijkl}^{qmm} H_k H_l + \ldots \tag{1.5}$$

where we have retained only terms up to the second order, although higher-order terms are expected to be significant in the appropriate experimental configurations. In Eqs. 1.3, 1.4, and 1.5, the superscripts of χ refer to the operator responsible for the electronic transition, both from absorption and emission, i.e., e represents electric dipole transitions, m magnetic dipole transitions, and q electric quadrupole transitions. When more than one component of the source $S_i(\mathbf{r}, t)$ is generated, the radiated fields add coherently, which can lead to interference effects.

We may read a term such as $\chi_{ijk}^{eem} E_j H_k$ in Eq. 1.3 as indicating two interactions of the incoming field with the material, one interaction with the electric field E_j and one interaction with the magnetic field H_k, while the left-hand side is proportional to the emitted radiation, i.e., $P_i \propto E_i$ of the radiated field. In the absence of absorption, energy and momentum must be conserved in this process, and the emitted photon may either carry the sum of the incident photon energies ($\omega_1 + \omega_2$) and be emitted in the direction $\mathbf{k_1} + \mathbf{k_2}$ or be emitted with the difference in their frequencies ($|\omega_1 - \omega_2|$) and be emitted in the direction $\mathbf{k_2} - \mathbf{k_1}$. Generally, both processes occur simultaneously with the overall radiation strength set by the corresponding susceptibility tensor element $\chi(\omega_1 + \omega_2, \omega_1, \omega_2)$ for the sum-frequency case and $\chi(|\omega_1 - \omega_2|, \omega_1, \omega_2)$ for difference frequency. In practice, the sum-frequency component is more readily measured.

Microscopically, the susceptibility tensor elements are given by terms as, e.g., [173],

$$\chi_{ijk}^{mem} \propto \sum_{g,n,n'} \left[\frac{\left(\widehat{M}_i\right)_{gn} \left(\widehat{P}_j\right)_{nn'} \left(\widehat{M}_k\right)_{n'g}}{\left(2\omega - \omega_{ng}\right)\left(\omega - \omega_{n'g}\right)} + \cdots \right] p_g^{(0)} \tag{1.6}$$

which in this example derives from absorption processes driven by the H-field polarized along k via the magnetic dipole operator $\left(\widehat{M}_k\right)_{n'g}$ between the ground state $|g\rangle$ and an intermediate excited state $|n'\rangle$ along with an electric dipole transition $\left(\widehat{P}_j\right)_{nn'}$ between the states $|n'\rangle$ and $|n\rangle$ via absorption of a j-polarized E field. Emission from $|n\rangle$ to $|g\rangle$ occurs via the magnetic dipole operator term $\left(\widehat{M}_i\right)_{gn}$ with a i-polarized H field. The denominator expresses the energy differences between the ground and excited states through ω_{ng} and the ground and intermediate states through $\omega_{n'g}$, while $p_g^{(0)}$ represents the thermal distribution of the ground state [53]. We note that the transition between the

intermediate states and the excited states does not form part of the resonance condition expressed in the denominator of Eq. 1.6.

Since the RA-NHG method depends upon an analysis of the susceptibility tensor elements, it is necessary to clarify which elements are present in bulk media. This is achieved by invoking Neumann's principle, which states that the physical symmetries of the crystal must be reflected in the transformation properties of its physical tensor properties. This constrains which elements of the susceptibility tensors in Eqs. 1.3, 1.4, and 1.5 are independent and nonzero. More precisely, under a unitary point transformation T_{ij} which leaves either the lattice, electronic, or magnetic order invariant, the corresponding optical susceptibility $\chi_{ijk\ldots}$ must also be invariant via

$$\chi_{mno\ldots} = \det(T)^{1+t} T_{im} T_{jn} T_{ko} \cdots \chi_{ijk\ldots} \tag{1.7}$$

We have explicitly enforced the constraint set by the parity of $\chi_{ijk\ldots}$ with respect to time reversal (either polar or axial) through the determinant of the transformation T with polar being even under time reversal and axial being odd. The symmetry of $\chi_{ijk..}$ is set by the product of its embedded electronic transition moment operators, as in Eq. 1.6: an even number of axial operators yields $t = 1$, while $t = 0$ for an odd number. We also note that other permutation symmetries of the indices are provided through time-ordering of the incident and emitted fields (i.e., Kleinman symmetry) and are only valid away from electronic resonance. Permutation symmetry due to degenerate incident fields further restricts the number and location of nonzero components probed in harmonic generation experiments. A full accounting of the above symmetries provides the full structure of the optical susceptibility tensors; these group theoretical considerations can be used in tandem with phenomenological models to reproduce NHG responses [65].

In the bulk response of centrosymmetric materials, odd-rank polar responses of electric dipole radiation are forbidden; for materials without a center of inversion, all responses are allowed. In all materials, the surface is a locus of inversion symmetry breaking, as are all interfaces between centrosymmetric media. All axial responses, such as emitted magnetic dipole operator (from the M_i terms in Eq. 1.4) or electric dipolar radiation which arises from an odd number of interactions with the magnetic component of the incident field with the material, are bulk allowed. Likewise, electric quadrupole radiation (from the Q_{ij} terms in Eq. 1.5) is bulk allowed in centrosymmetric materials. These sources of radiation are generally quite weak, although they may be made more visible upon resonant enhancement.

In practical terms, we note that the emitted electric dipole response is by far the most commonly observed RA-NHG response. However, there are notable examples in the literature where the magnetic dipole response M_i is dominant, which includes a resonant transition involving the magnetic dipole operator. The electric quadrupolar response due to the Q_{ij} terms in Eq. 1.5 is also reported in the literature. However, due to the gradient term for quadrupole radiation present in Eq. 1.2, the magnitude of the emitted radiation is weak and may be significantly weaker than the third harmonic generation although they report tensors of equal rank.

4.1.1 Effect of Static Fields

While it is generally true that an increase in tensor rank corresponds to a higher harmonic, there are exceptions beyond higher-order multipolar radiation. Static externally applied or internal fields can modify RA-NHG measurements by increasing the order of the interaction (and thus rank of susceptibility tensor probed) by one without increasing the energy of the emitted photon. For magnetic fields in the linear optical field approximation, this is the origin of the Faraday effect

$$P_i(\omega) = \chi_{ijk} E_j(\omega) B_k(0) \tag{1.8}$$

where the second-order interaction between the static magnetic field and optical field at frequency ω reveals tensor elements of the axial tensor χ_{ijk} allowed for inversion symmetric materials. The typical result is an optical birefringence that effectively rotates the polarization of the light by an angle proportional to the external field $B_k(0)$. This effect can be exploited for RA-NHG experiments by inducing the axial tensor associated with magnetic field-induced second harmonic (MFISH):

$$P_i(2\omega) = \chi_{ijkl} E_j(\omega) E_k(\omega) B_l(0). \tag{1.9}$$

Similarly, a static electric field may either be applied or arise internally in a sample as a result of, e.g., charge accumulation on the surface or a spatial dependence of the band structure. The result is electric field-induced second harmonic (EFISH):

$$P_i(2\omega) = \chi_{ijkl} E_j(\omega) E_k(\omega) E_l(0) \tag{1.10}$$

which is a polar response and can induce a bulk second harmonic generation from inversion symmetric materials.

A similar line of reasoning may be applied to magnetic ordering in materials. In this case, the electric and magnetic susceptibilities are modified by the presence of a static bulk magnetization **M**, and we may consider, for example, the second-order optical susceptibility $\chi_{ijk}(\mathbf{M})$ which may be expanded in powers of M as

$$\chi_{ijk}(\mathbf{M}) = \chi_{ijk} + \chi_{ijkl} M_l + \chi_{ijklp} M_l M_p + \chi_{ijklpr} M_l M_p M_r + \ldots \tag{1.11}$$

The zeroth-order term in Eq. 1.11 is the crystallographic term of Eqs. 1.3, 1.4, and 1.5. The higher-order terms in the magnetization can thus induce additional RA-NHG responses which coherently interfere with the bare lattice contribution. In principle, the effect of a finite magnetization is valid at arbitrary order in the optical fields, where we note that it is most efficient for magnetic effects whose axial tensors are allowed at all even orders for inversion symmetric materials.

4.1.2 Rotational Anisotropy Signal

Once the relevant responses are categorized and understood, it is possible to compute the signal. As described below, there are three experimental geometries to access the

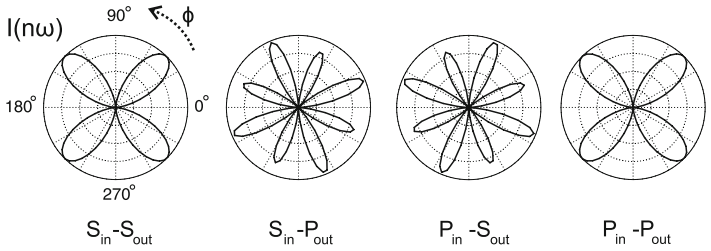

Fig. 1.1 Simulated RA-THG data for the 4/*m* (C_{4h}) point group (Figure from Ref. [184])

elements of $\chi_{ijk\ldots}$ which operate either by rotating the sample with respect to the scattering plane or by rotating the incoming and/or outgoing polarization of the fields. In the former case, the signal is computed by explicitly calculating the relevant response from each source term in Eq. 1.2, for example, $\chi^{eee}_{ijk} E_j E_k$ for bulk electric dipole radiation, on a susceptibility tensor which has been rotated by an arbitrary angle ϕ, e.g., about the z-axis (z being coincident with the sample normal) as

$$T_{ij} = \begin{pmatrix} \cos(\phi) & -\sin(\phi) & 0 \\ \sin(\phi) & \cos(\phi) & 0 \\ 0 & 0 & 1 \end{pmatrix}. \tag{1.12}$$

In the latter case, the rotation operation is performed upon the fields and not the susceptibility tensor.

There are a number of experimental geometries, described below, which access the nonlinear response and measure its anisotropy as a function of either the sample rotation or field polarization angle. A simulated example is shown in Fig. 1.1 for third harmonic generation at oblique incidence, yielding rotational anisotropy third harmonic generation data (RA-THG). In the figure, we have denoted the incoming and outgoing polarizations as p or s depending upon whether they are either polarized in or out of the plane of incidence. The radiated patterns reflect the underlying symmetry being probed via the combination of nonzero tensor elements present in their calculated expressions, e.g., if the material has fourfold symmetry, the resulting patterns should be fourfold rotationally symmetric, etc.

When appropriately modeled, fits to the rotational anisotropy patterns can deduce the tensor elements present in the nonlinear response. From this, one can deduce the crystalline point group symmetry, the magnetic point group symmetry, and/or the presence of other previously inaccessible electronic transitions. Examples of this form of analysis are given in Sect. 3.1.

4.2 Optical Setups

RA-NHG experiments have so far been conducted in one of three sample geometries, depicted in Figs. 1.2, 1.3, and 1.4. The first geometry shown in Fig. 1.2 is

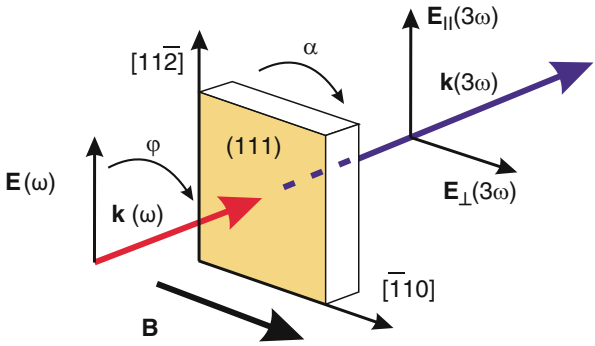

Fig. 1.2 First experimental RA-NHG geometry described in the text where the beam is normally incident upon the sample (Figure reproduced from Ref. [114])

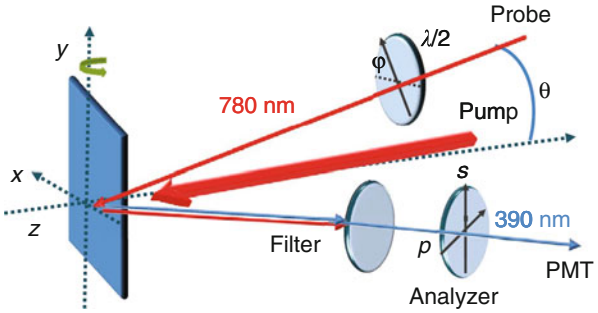

Fig. 1.3 Second RA-NHG geometry where the beam is obliquely incident upon the sample and rotational anisotropy is recorded by rotating the wave plate and analyzer. Note the presence of a "pump" beam which may be used in time-resolved experiments, discussed below (Figure reproduced from Ref. [176])

appropriate for flat, transparent materials. Here, the beam is normally incident and focused upon the sample, and the incident polarization is set by the combination of a half wave plate and polarizer. An analyzer is used to select the outgoing polarization, which is chosen either parallel or perpendicular to the incident polarization. The polarizer and analyzer are then rotated by an angle ϕ (the wave plate by an angle $\phi/2$), and the rotational anisotropy of nonlinear harmonic generation is measured by spectrally filtering the desired harmonic and measuring its intensity. This configuration is easy to align and can be performed on small samples. Because the sample is stationary in this geometry, it may be measured in a variety of environments including at low temperatures or in magnetic fields. However, the consequence of normal incidence is that there is no distinction between p and s polarizations limiting the range of accessible tensor elements and optical transparency is necessary.

The second geometry, suitable for reflective samples, is shown in Fig. 1.3. In this case, the incoming field is obliquely incident relative to the normal face of the sample. A polarizer is used to purify the incident polarization and an analyzer is used to select the output polarization. Owing to the oblique incidence of the light, there is

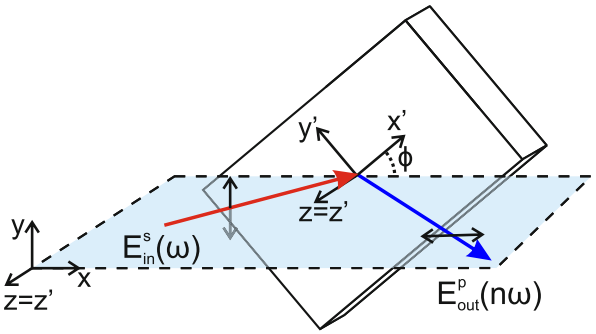

Fig. 1.4 Schematic depiction of the third experimental geometry. The scattering plane is represented in sky blue with the incoming (*red*) and outgoing fields (*dark blue*) denoted by arrows lying totally in, and thus defining, the plane. S polarization is perpendicular to the plane, while p polarization is fully in the plane. ϕ denotes the angle that the crystalline axis x' subtends with respect to the scattering plane axis x for rotation about the $z = z'$ axis (Figure reproduced from Ref. [184])

a well-defined scattering plane and thus well-defined s-polarized and p-polarized fields for both incoming and outgoing fields. The p-polarized beam has a component of the electric field parallel to the sample normal, allowing access to a larger collection of tensor elements. The polarizations of the incoming and outgoing electric fields are then rotated while the sample remains stationary, forming a "map" of the rotational anisotropy as a function of both rotation angles. The advantage of this approach is that it permits easier determination of the lattice or magnetic symmetry of the material being studied as compared with the previous experimental geometry. It is similarly easy to align as the prior configuration, although some tensor components are not accessed due to the scattering plane being fixed with respect to the crystalline axes, limiting the extent to which symmetries can be determined.

Access to the largest number of tensor elements may be achieved using the third experimental geometry, shown in Fig. 1.4 in which light is introduced at oblique incidence to define a scattering plane. The sample is rotated about an axis lying in this scattering plane. In this case nearly all tensor elements are recovered when incident and outgoing fields are cycled for all available polarization combinations; all may be recovered if more than one sample face normal is measured. However, there are a number of experimental complications which have made use of this experimental geometry difficult. An optically flat portion of the sample must be positioned on the axis of rotation of its stage to within a fraction of the incident beam diameter (typically of order 10–50 μm). This is necessary to avoid beam walkoff or signal artifacts due to sample inhomogeneity over the full 2π rotation; otherwise only spatially homogeneous and flat materials may be studied, such as thin films. For cryogenic measurements, the experiment requires that the sample is affixed to a rotation stage to rotate it. This stage may lay atop a series of mechanical stages to position the sample appropriately, which may result in lost cooling power for cold-finger cryostats (although not for sample-in-vapor cryostats). Magnetic field-dependent measurements can only be made with the sample rotating with respect

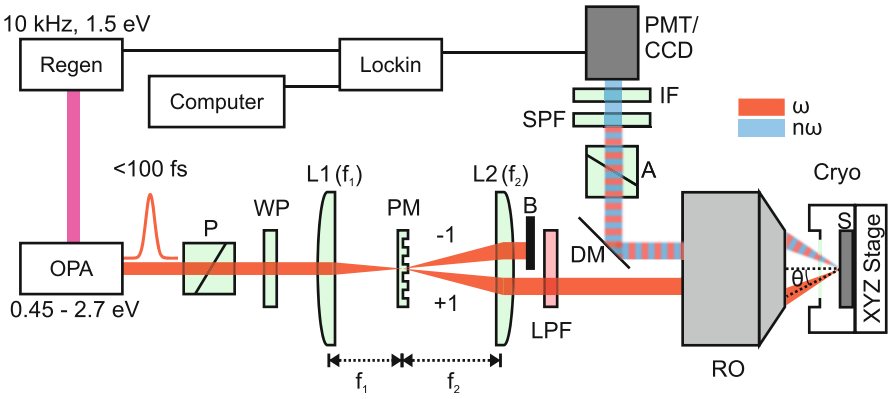

Fig. 1.5 Top-down schematic layout of the setup developed by the authors showing all relevant optics. These optics are polarizer (*P*), wave plate (*WP*), first lens (*L1*), phase mask (*PM*), second lens (*L2*), black tape (*B*), long-pass filter (*LPF*), reflective objective (*RO*), d-cut mirror (*DM*), analyzer (*A*), shortpass filter (*SPF*), and interference filter (*IF*). The detector used for quantitative measurement was a photomultiplier tube (*PMT*). The sample (*S*) is depicted in its cryostat, which was mounted on an XYZ stage. Also represented are the laser (ReGen), OPA, detection electronics (lock-in), and computer (Figure reproduced from Ref. [184])

to a static background magnetic field since the field and sample do not rotate together without the use of a rotatable vector magnet. Unconventional experimental geometries, such as those requiring externally strained samples, may not be easily employed using this scheme due to the need for sample rotation. Finally, we note that precession of the sample normal about the rotation axis relative to the scattering plane may also result in experimental artifacts.

A recent development by the authors allows for the rotation of the scattering plane thus permitting access to the maximal number of available tensor elements but without the need to attach the sample to a rotation stage [184]. The setup, shown in Figs. 1.5 and 1.6, relies upon imaging a diffractive binary phase mask onto the sample to provide an incident angle which defines a scattering plane. As the diffractive optic is rotated, the scattering plane is rotated and the return beam is captured by a rotating detection arm. This geometry allows for examination of small samples, as a local probe, for samples in cryogenic conditions and in magnetic fields.

4.2.1 Light Sources and Detection

The choice of laser is a balance between peak field intensity and spectral resolution. The wavelength should also be selected appropriately because it influences which electronic transitions are accessed through Eq. 1.6. Because $\chi^{(2)}$ is small for most materials, pulsed sources are preferred over continuous-wave ones. Ultrafast ~ fs pulse-duration sources can drive a higher degree of nonlinearity for a low amount of average power. These include Ti/sapphire-based oscillator and amplifier sources with a native wavelength of 800 nm corresponding to 1.5 eV. These can further drive parametric devices allowing wavelength tunability extending from 20 μm to

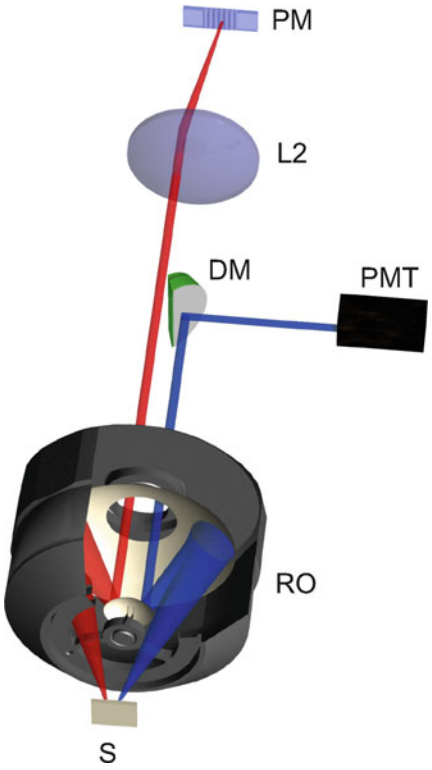

Fig. 1.6 Perspective schematic depiction of the authors' RA-NHG system. Shown here are the diffractive binary phase mask (*PM*), beam block (*B*), collimating lens (*L2*), Cassegrain reflective objective (*RO*), sample (*S*), d-cut mirror (*DM*), and PMT. The dashed arrows show which optics move, with all axes of rotation coincident with the optical axis. We note that the wave plate (not shown) must also rotate to set the appropriate polarization. (Figure reproduced from Ref. [184])

~200 nm. However, spectral resolution for spectroscopic measurements may require ~ ps or ns sources, requiring much large pulse energies. They can also be made to drive wavelength tunable devices, albeit over a narrower range.

After it has been generated, the higher harmonic light must be separated from the fundamental frequency in order to be detected background free. One choice is to use optical filters made of absorptive glasses or covered with special dielectric coatings, e.g., shortpass or bandpass filters. We note that it can often take a number of successive filters to adequately remove the fundamental background in the beam. In some cases, the spectral separation may also involve a commercial monochromator or a dispersing prism and iris combination. In this case, either the intensity or the radiated spectrum may be measured.

Choice of the detector and supporting electronics depends upon the level of generated light and the wavelength being detected. In experiments where the material being studied breaks inversion and the interaction length between material and field is

long, a simple photodiode may be used in conjunction with lock-in detection. However, even in these cases, there is generally a need for highly sensitive detectors. Photomultiplier tubes have long been the tool of choice and may be used in either analogue mode (i.e., to provide a current or voltage) or photon counting mode along with photon counting electronics. These detectors generally have their maximum response in the boundary between the visible and UV portion of the spectrum. Semiconductor-based avalanche photodiodes may also be used in photon counting mode using photon counting electronics. Their primary advantage is that they may be used for a wider range of emitted photon energies, being suitable for detection from 300 nm to 1.7 μm depending upon the detector material. High quantum efficiency CCD cameras can also be used for detection of light intensity, as detectors at the end of monochromators for spectroscopic measurements, and as a means of SHG imaging.

4.2.2 Time Resolution

When studied using femtosecond lasers, RA-NHG methods may be incorporated into time-resolved pump-probe techniques to interrogate the transfer of energy between degrees of freedom of a system, examine photocarrier relaxation, and even resolve ultrafast symmetry changes. In these methods, a short (i.e., fs or ps timescale) "pump" pulse drives the system out of equilibrium, and the return to the equilibrated state is monitored in the time domain with a separate, time-delayed field. The probing is then selected for the nonlinear harmonic response depending upon the degree of freedom being selected, e.g., surface, structural, or magnetic ones.

5 Key Research Findings

5.1 Crystallographic Measurements of Hard Condensed Matter

Below, we review the most recent experimental findings using the RA-NHG technique since 2009, broadly classified within studies which primarily examine the lattice (crystallographic) and those which probe electronic and magnetic order. Our approach will be to summarize findings in a number of subtopics, each selected to highlight a particular application as an example of the RA-NHG technique. Other works which fit within each topic are also very briefly discussed. Specifically, we will describe the study of the surface states of Bi_2Se_3 in Sect. 3.1.1 and the structural refinement of a centrosymmetric crystal in Sect. 3.1.2. Section 3.1.3 will describe the application of a non-degenerate, rotational anisotropy sum-frequency generation measurement to determine adsorbed molecular dynamics. Other examples of interface physics are also mentioned. Sections 3.1.4 and 3.1.5 describe RA-SHG measurements on 2D materials. The application of RA-SHG as an imaging modality is described in Sects. 3.1.6 and 3.1.7. A number of applications of RA-SHG to nanostructures are also briefly mentioned in Sect. 3.1.6.

We wish to emphasize that what is described in detail below is not an exhaustive treatment of RA-SHG measurements across all disciplines. There are several

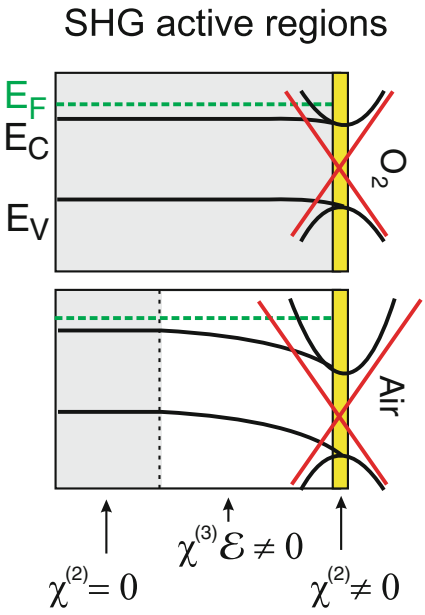

Fig. 1.7 Schematic depiction of band bending in Bi_2Se_3. A space-charge layer builds on the surface due to migration of Se atoms. When the material is cleaved in the presence of oxygen, there is no bending at the surface (Figure taken from Ref. [78])

applications of RA-SHG to biological systems as an imaging modality, and we refer the reader to the appropriate recent literature [1, 18, 28, 43, 70, 75, 92, 108, 120, 127, 130, 140, 160, 162, 170, 180–182, 187, 188, 205, 223, 224].

5.1.1 Changes in Electronic Structure: The 3D Topological Insulator Bi_2Se_3

Bi_2Se_3 is a 3D topological insulator with linearly dispersing protected surface states arising from strong spin-orbit coupling in the bulk band structure. While nominally bulk insulating, it is doped into a conductor by Se vacancies making the electronic properties of the conducting topological surface states difficult to separate from the bulk. As a centrosymmetric crystal (point group class C_{3v}), the surface selectivity of electric dipolar second harmonic generation provides an opportunity to study the surfaces of Bi_2Se_3 single crystals free of interference from the bulk.

Hsieh et al. measured the time-dependent RA-SHG of freshly cleaved Bi_2Se_3 on minute-long timescales. The data revealed that upon a fresh cleave, the bulk band structure "bends" in the vicinity of the surface due to migration of negatively charged Se vacancies to the surface on the timescale of ~100 min [78]. This "band-bending" effect serves as an effective bias which breaks inversion on the order of 2 nm into the bulk as depicted schematically in Fig. 1.7 and results in an EFISH signal superposed upon the dipolar surface SHG signal in the RA-SHG traces. However, despite this complication, the surface can still be probed by second harmonic generation provided that the surface contribution is appropriately separated from the bulk contribution through fitting, and the authors demonstrated that dosing the surface with O2 could recover the initial uncleaved state of the material. A

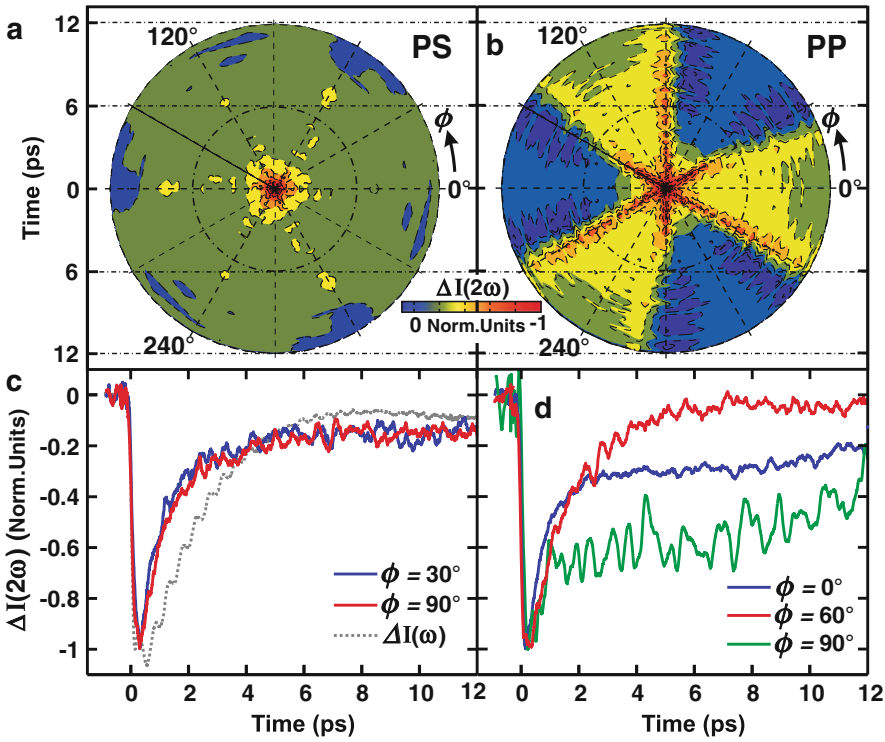

Fig. 1.8 Time-resolved response of the relative change in the RA-SHG response is shown in (**a**) $\Delta I_{ps}(2\omega)$ and (**b**) $\Delta I_{pp}(2\omega)$. Cuts along specific directions for the two responses are shown in (**c**) and (**d**) (Figure taken from Ref. [77])

follow-up study by McIver et al. incorporated a theoretical model based upon these findings and a more detailed analysis of the optical properties of Bi_2Se_3 in order to separate the surface SHG and space-charge layer inducing EFISH contributions [133], while a more detailed examination of the origin and effects of band bending was examined by Xu and coworkers [212].

Hsieh et al. later extended the above measurements to time-resolved dynamics of photoexcited Bi_2Se_3 using RA-SHG as a probe [77]. The resulting time-domain dynamics are shown in Fig. 1.8, where normalized time and angle resolved plots of $\Delta I_{pp}(2\omega)$ and $\Delta I_{ps}(2\omega)$ are shown. Through careful analysis of the recovery dynamics, the authors determined that the in-plane surface carriers relax quickly through intraband cooling (<2 ps), whereas the space-charge layer dynamics are significantly slower (~21 ps). The authors then compared the results of the charge decay to the spin dynamics accessed through the time-resolved second harmonic magneto-optical Kerr effect and observed that the spin dynamics of the surface carriers decays within 0.2 ps, markedly faster than the charge degree of freedom.

5.1.2 Structural Refinement: The 5d Transition Metal Oxide Sr_2IrO_4

Determining structural symmetry is a common application of SHG. It is most easily applied to distinguish between centrosymmetric and inversion symmetry-breaking structures due to the dipole-forbidden radiation of the former and dipole-allowed SHG of the latter. This approach does not usually necessitate the use of rotational anisotropy, as the onset of the inversion symmetry-breaking phase is usually accompanied by a marked increase in the SHG response of beams in a particular scattering plane, and thus the rotational information is unneeded and a simpler experiment can be performed. However, the application of the RA-SHG technique can provide a clear roadmap to a structural point group symmetry of the lattice [53, 193]. In recent years, it has been applied to mixed structural symmetries and crystalline orientations [95, 111] as well as organic crystals [194] and microcrystals [192].

As an application, we consider the 5d transition metal oxides. A variety of novel quantum ground states may exist in these materials due to their unique interplay between crystalline electric field, spin-orbit coupling, and electronic correlation [206]. Currently, the most widely studied materials based on 5d elements are the iridates. Within this class, Sr_2IrO_4 has been a focal point of scientific inquiry because of its structural and magnetic similarities to the copper-based superconductor La_2CuO_4, which has led a number of authors to posit that if appropriately doped, Sr_2IrO_4 should exhibit superconductivity, similar to the cuprate [129, 135, 199, 204].

However, the details of these predictions, as well as a number of phenomenological observations of the physics of Sr_2IrO_4, are contingent upon a proper understanding of the lattice and magnetic symmetries. Specifically, the originally accepted structural symmetry of Sr_2IrO_4 in Fig. 1.9a is a layered perovskite structure where the iridium ion is centrally located within corner-sharing, canted oxygen octahedra. In contrast, the octahedra in La_2CuO_4 are not canted. Upon magnetic ordering, the spin-orbit coupled $J_{eff} = 1/2$ pseudospins in Sr_2IrO_4 antiferromagnetically align at the Neel temperature $T_N = 240\,\mathrm{K}$ in a manner in which they are locked to the canted octahedra. Since both materials are Mott insulators below T_N, the structural, magnetic, and electronic similarities allow a mapping of Sr_2IrO_4 onto La_2CuO_4 with the implication that the former should exhibit unconventional superconductivity mediated by fluctuating $J_{eff} = 1/2$ pseudospin order, similar to antiferromagnetic spin fluctuation-mediated superconductivity in doped La_2CuO_4.

However, the structural symmetry portrayed in Fig. 1.9a has been called into question in recent years by neutron scattering measurements which show weak nuclear Bragg reflections not consistent with the original structural refinement [41, 216]. This picture is obscured by the iridium atom's high neutron absorption cross section compounded with the fact that currently available single crystal samples are small relative to the neutron beam. A full point group symmetry assignment can be made using RA-SHG in Sr_2IrO_4, provided that the bulk quadrupolar response is measured.

The authors of this review applied their RA-NHG spectrometer of Figs. 1.5 and 1.6 to oriented Sr_2IrO_4 crystals in both the second and third harmonic channel [184, 185]. The RA-SHG signals shown in Fig. 1.9b and c were determined to derive solely from bulk quadrupolar second harmonic generation. The results indicate a

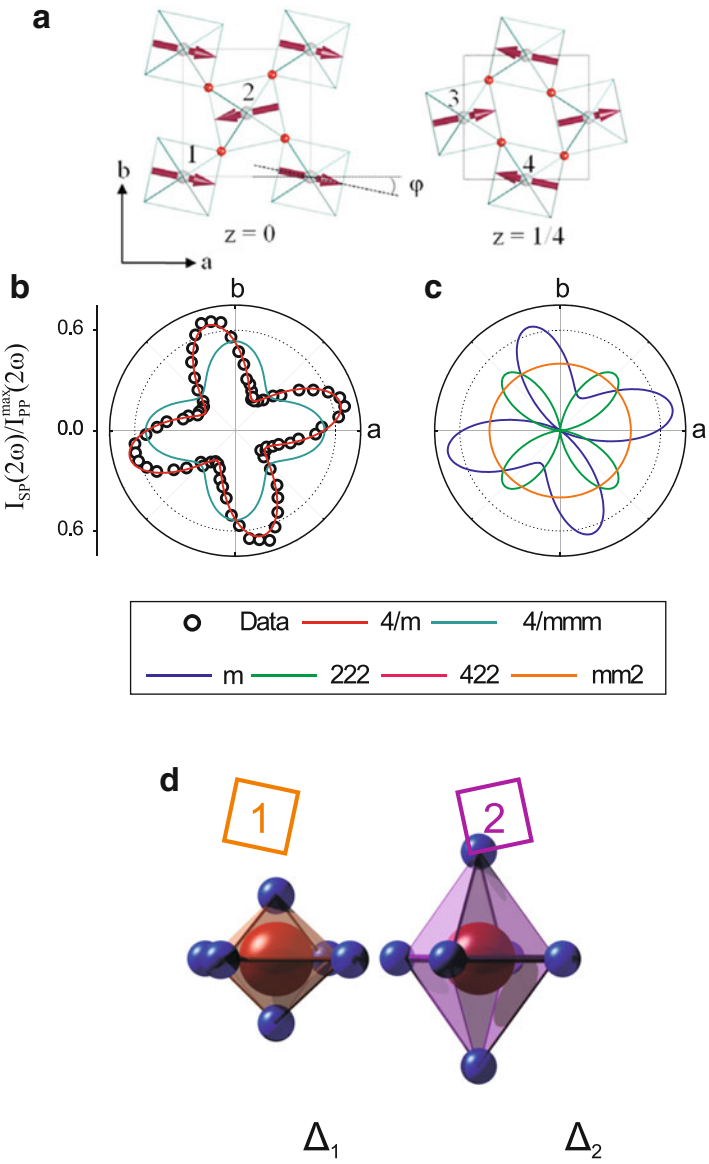

Fig. 1.9 (**a**) Initially refined crystallographic and magnetic structure of Sr_2IrO_4 showing the canted, corner-sharing oxygen octahedra of the crystal structure. In the original structural refinement, the two sublattices, i.e., of the clockwise canted and the counterclockwise canted octahedra, share the same dimensions. (**b**) RA-SHG scan in the s-in p-out geometry for Sr_2IrO_4 with fits to the D_{4h} (4/mmm) and C_{4h} (4/m) point groups. The data are uniquely consistent with quadrupolar SHG originating from the C_{4h} (4/m) point group. (**c**) Fits to a variety of other point groups are markedly inconsistent with the data. (**d**) Staggered distortion of the oxygen octahedra in Sr_2IrO_4. The staggered distortion actually allows the magnetoelastic locking seen in (**a**) (Panel (**a**) taken from Ref. [14] and panels (**b**–**d**) taken from Ref. [185])

lowering of the bulk symmetry from the initial posited point group (D_{4h}) to C_{4h} due to the loss of two glide planes in the material which arises from a staggered distortion of the two sublattices of the crystal, as shown in Fig. 1.9d. The authors then carefully modeled the impact of this staggered distortion on the magnetic structure and deduced that it allows the spins to lock to the octahedra.

5.1.3 Surface and Interface Characterization: Rotational Anisotropy Sum-Frequency Generation as a Probe of Adsorbed Molecular Motion

The interface is the locus of inversion symmetry breaking between two centrosymmetric materials and is thus ideally suited to study by second-order spectroscopies. In recent years, RA-SHG and its analogues have found myriad uses in applications to interface physics through synergistic approaches with time-resolved methods to examine charge migration in semiconductors [143], measurement of inhomogeneities and magnetic properties of oxide interfaces [52, 64, 145], SHG enhancement at buried magnetic interfaces [161], characterization of liquid/liquid [148, 183] interfaces, observation of plasmonic hotspots in metallic films [13], measurement of charge separation at inorganic/organic interfaces [151], characterization of electronic defects and charge traps at Si/SiO_2 interfaces [142, 150, 151], dynamics at GaAs/GaSb/InAs and GaAs/GaSb heterostructures [59], and its usage as a tool to characterize the enhancement of SHG from anodic oxide films on $Hg_{1-x}Cd_xTe$ (MCT) substrate [202].

As a probe of surface properties, RA-SHG measurements have recently been applied to a variety of coated semiconductors and thin films, including the properties of air/water [54, 113, 121, 128, 203, 214] and air/liquid [123] interfaces, molecular adsorption [60, 138, 215, 225], characterizing Fe/AlGaAs (001) heterostructures for use in SHG-detected coherent acoustic phonon experiments [219], molecular orientation in self-assembled multilayers [198], properties of polymer thin films [85, 89, 91, 156], studying passivation of GaAs surfaces [56, 57] and oxide-covered Ge(111) and Ge(100) [158], observation of multipolar SHG enhancement from surface morphology [200], measuring SHG as a function on Si content in SiN_x thin films [102] and quantifying the multipolar SHG emitted from interaction of a Gaussian beam with a SiN film [81], examining both clean and hydrogen-covered vicinal Si(001) surfaces [47], determining the orientation of oblique angle deposited SiO thin films [4], and characterizing α-CN-terthiophene thiolate films on GaAs(110) [118].

Rather than second harmonic generation, we take as an instructive example the case where the incident fields are non-degenerate in energy and wave vector. The emitted sum-frequency generation (SFG) is measured as a function of rotation of the sample relative to the incoming non-degenerate fields. This approach is particularly useful when studying the vibrational and rotational motions of adsorbed molecules and their interaction with a crystalline substrate: one of the incoming fields can be made resonant to the mode being studied, while the second field can serve the dual role of upconverting the signal to a measurable wavelength range and, since the second-order effect is electric dipole forbidden in the bulk, allow for measurement of a surface selective response. The

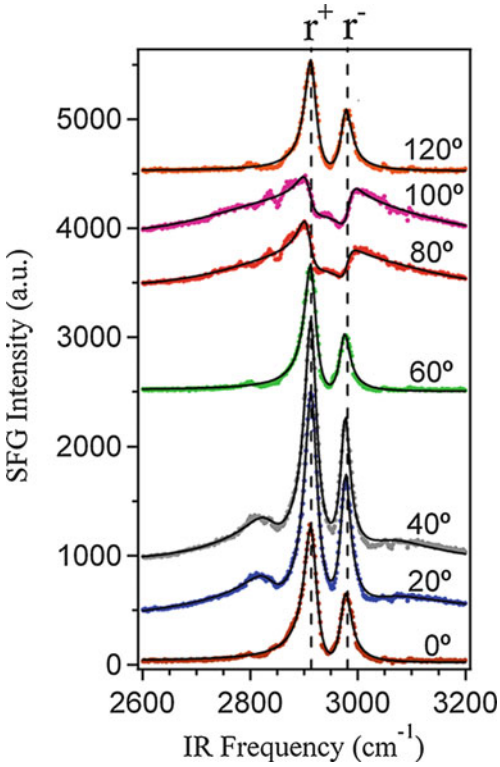

Fig. 1.10 SFG PPP spectra in methyl-terminated Si as a function of angle. Fits to Eq. 1.13 are shown as *black lines* through the data (Figure taken from Ref. [125])

recorded SFG signal can then be spectrally dispersed and analyzed in the frequency domain to provide lifetime information on the mode being studied.

Examples include revealing the molecular orientation at interfaces [197] or the presence of a surface quadrupole in ice [177]. Malyk et al. applied rotational anisotropy SFG to measure the modification of rotational and vibrational dynamics of methyl groups due to terminating the Si(111) surface [125]. In this latter work, which we focus on here, the SFG response for incident radiation resonant with vibrational dynamics is modeled as a sum of a nonresonant contribution and vibrational modes by

$$I^{SFG} \sim \left| A_{NR} e^{i\phi} + \sum_{j=1}^{N} \frac{B_j}{\omega - \omega_j + i\Gamma_j} \right|^2 e^{-(\omega-\omega_g)^2/\sigma^2} \tag{1.13}$$

where ω is the wavelength; A_{NR} and ϕ, respectively, represent the amplitude and phase of the nonresonant response; B_j is the amplitude and Γ_j the linewidth of the Lorentzian describing the vibrational mode; and the spectrum of the laser pulse is modeled as a Gaussian in frequency with central frequency ω_g and width σ.

An example of SFG traces acquired at 20° rotational increments of the substrate is shown in Fig. 1.10, where two peaks are visible: the CH3 symmetric stretch (r^+) at

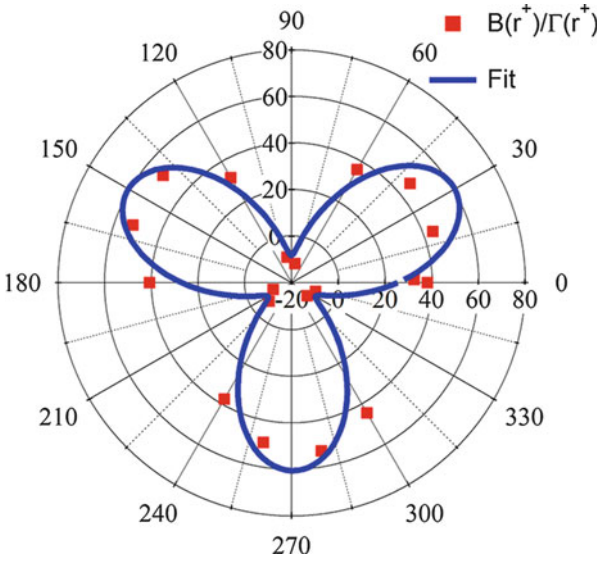

Fig. 1.11 SFG PPP rotational anisotropy data in methyl-terminated Si as a function of angle. The data points are the peaks (Figure taken from Ref. [125])

2912 cm^{-1} and the CH3 asymmetric stretch (r^-) at 2976 cm^{-1}. As the sample is rotated, the peak strengths and widths are modulated in a manner which reflects the underlying threefold symmetry of the Si(111) surface. This can be clearly seen for the symmetric stretch (r^+) in a plot of the fitted peak magnitudes as a function of sample rotation angle, shown in Fig. 1.11. The authors proceed with a detailed analysis of the discrepancy in linewidth of the CH_3 asymmetric stretch in two different polarization combinations (PPP and SPS, where the polarizations are labeled in order of radiated, incoming visible and incoming IR field). Their analysis of the linewidth reveals that the rotational motion of the methyl group is hindered due to adsorption onto the Si(111) substrate; rather than rotation occurring on the 100 fs observed for free methyl rotors, it occurs on a 1–2 ps timescale.

5.1.4 Influence of Current Biasing on 2D Materials: Graphene

Graphene is a single layer of carbon atoms arranged in a hexagonal lattice whose carriers derive from linearly dispersing bands at the k and k' points of the Brillouin zone. These massless Dirac fermions lie at the heart of many of graphene's favorable transport properties, making it an excellent candidate for next-generation electronic devices. While electric dipole SHG is forbidden from free-standing graphene, when either grown or transferred onto a substrate, the interface is a locus of inversion breaking that can produce an isotropic SHG response derived from the graphene itself.

Dean and van Driel applied RA-SHG measurements to exfoliated graphene and graphitic films to demonstrate its sensitivity to single and multilayer stacking [35], which they later described within the framework of a detailed theoretical model [36]. Due to the registry between graphene and charge neutral, dielectric hexagonal BN, the latter has often been used as a substrate for the former, attracting RA-SHG

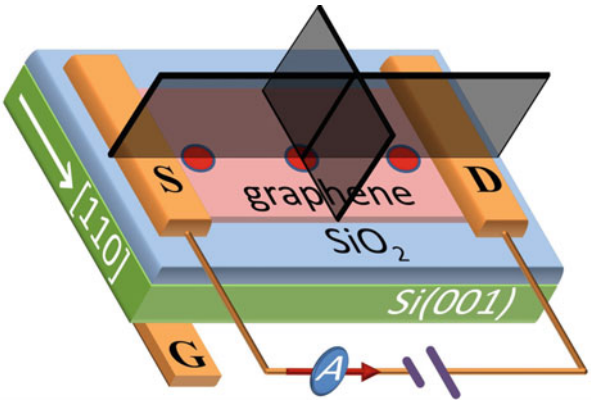

Fig. 1.12 Experimental configuration in Refs. [2] and [3]. The patterned electrodes of the source (*S*) and drain (*D*) are shown. There is also a back gate (*G*). The two mirror planes are depicted for the unbiased system (Figure taken from Ref. [3])

characterizations of h-BN bilayers and multilayers [97, 119, 147]. In later studies, Bykov et al. experimentally revealed an enhancement of SHG from multilayer graphene as a function of applied current [22], predicted theoretically for bilayer graphene by Wu et al. [207].

An et al. extended these measurements by studying the effects of biasing graphene deposited on SiO_2/Si(001) [2, 3] and a 3.5°-miscut vicinal SiC(0001) [3] substrate to uncover the origin of the 30 % enhancement of SHG from passing a current through the material. The use of RA-SHG in the oblique incidence geometry shown in Fig. 1.12 allows for the separation of the contribution from the Si(001) surface at its interface with graphene: the rotationally isotropic response derives from graphene, whereas all of the anisotropy as a function of scattering plane rotation arises from the underlying substrate.

As a result, the second harmonic signal should take the form

$$I_{pp}(\phi) = |a_0 + a_4 \cos(4\phi)|^2 \tag{1.14}$$

where the isotropic term a_0 derives from both the graphene layer and the Si(001) surface, whereas a_4 is the coefficient of the anisotropic term due to the Si(001) surface alone. In the presence of a current, the isotropic term is modified to

$$a_0 = a_0^{Si} + a_0^C + \sum_{n=0}^{3} a_n^I I \cos[n(\phi + \pi/2)] \tag{1.15}$$

where a_0^{Si} derives from the SiO_2/Si interface, a_0^C derives from the graphene layer, and a_n^I arises from the current.

The authors' findings for both materials are mutually consistent and thus we focus on the material deposited on SiO_2/Si(001). Figure 1.13 shows that as a positive current is applied, the sign of the isotropic piece of the graphene SHG switches from positive to negative. This response is not uniform, as Fig. 1.14 shows that the RA-SHG patterns are positionally dependant as a function of distance between the